AGU PUBLICATIONS

JGR

Journal of Geophysical Research: Space Physics

RESEARCH ARTICLE
10.1002/2017JA023991

Key Points:
- We compare average nightside aurora of different magnetospheric modes (substorms, steady magnetospheric convection events, and sawtooth events)
- Steady magnetospheric convection events produce brighter aurora than substorms, but sawtooth events are the brightest overall
- Despite much higher magnetospheric driving of sawtooth events, the aurora takes half the time to dim than after substorms

Supporting Information:
- Supporting Information S1
- Movie S1
- Movie S2
- Movie S3
- Movie S4
- Movie S5
- Movie S6
- Text S1

Correspondence to:
M.-T. Walach,
m.walach@lancaster.ac.uk

Citation:
Walach, M.-T., S. E. Milan, K. R. Murphy, J. A. Carter, B. A. Hubert, and A. Grocott (2017), Comparative study of large-scale auroral signatures of substorms, steady magnetospheric convection events, and sawtooth events, *J. Geophys. Res. Space Physics*, *122*, doi:10.1002/2017JA023991.

Received 7 FEB 2017
Accepted 8 JUN 2017
Accepted article online 12 JUN 2017

Comparative study of large-scale auroral signatures of substorms, steady magnetospheric convection events, and sawtooth events

M.-T. Walach[1,2], S. E. Milan[1], K. R. Murphy[3], J. A. Carter[1], B. A. Hubert[4], and A. Grocott[2]

[1]Department of Physics and Astronomy, University of Leicester, Leicester, UK, [2]Physics Department, Lancaster University, Lancaster, UK, [3]NASA Goddard Space Flight Center, Greenbelt, Maryland, USA, [4]Laboratoire de Physique Atmosphérique et Planétaire, University of Liège, Liège, Belgium

Abstract This paper investigates the auroral evolution during different magnetospheric modes: substorms, steady magnetospheric convection, and sawtooth events. We undertake a superposed epoch analysis using data from the Imager for Magnetopause-to-Aurora Global Exploration Far Ultraviolet spectrographic imager and wideband imaging camera for each of these event types. We find that the auroral oval narrows and shows an equatorward movement prior to substorm onset. At substorm onset, the auroral oval brightens explosively near 23 magnetic local time (MLT). After this the aurorae expand poleward and the brightening stretches duskward and dawnward, with the duskward expansion being faster. Approximately 20 min after substorm onset, the aurorae begin to dim. Steady magnetospheric convection events with preceding substorms initially show the same signatures as substorms, but instead of the recovery after 20 min postonset, the aurorae stay bright for an extended period of time (at least 4 h after onset). Despite continued dayside driving of the system during steady magnetospheric convection events, we see a reconfiguration in the nightside auroral activity, taking place between 120 to 150 min after onset. Sawtooth events show very similar signatures to substorms, except for the auroral emission being much brighter, covering a wider MLT extent, and taking significantly less time to recover. The proton aurorae during substorms take ~2–4 h to dim, during sawtooth events this process takes less than 1 h, despite enhanced reconnection rates. A similar effect is seen in the electron aurorae, albeit not as extreme.

1. Introduction

When the interplanetary magnetic field (IMF) points southward ($B_Z < 0$), reconnection at the dayside magnetopause opens terrestrial magnetic flux, which then convects over the polar regions toward the nightside magnetosphere where it can close again [*Dungey*, 1961, 1963; *Cowley and Lockwood*, 1992; *Lockwood and Cowley*, 1992; *Cowley and Lockwood*, 1996; *Milan et al.*, 2003, 2007; *Milan*, 2015]. This cycle of opening and closing of magnetospheric flux, driven by reconnection, is known as the Dungey cycle. The rate of change of polar cap flux, or the rate of change of the amount of open magnetospheric flux, $\frac{dF_{PC}}{dt}$, is given by

$$\frac{dF_{PC}}{dt} = \Phi_D - \Phi_N, \quad (1)$$

where the dayside and nightside rates of reconnection, Φ_D and Φ_N, are time-dependent variables [*Siscoe and Huang*, 1985; *Cowley and Lockwood*, 1992; *Lockwood and Cowley*, 1992; *Milan et al.*, 2003, 2007, and references therein].

The rate at which magnetospheric flux is opened at the dayside, Φ_D, is dependent on the solar wind conditions [*Caan et al.*, 1977; *Perreault and Akasofu*, 1978; *Milan et al.*, 2012, and references therein], whereas the rate at which open flux is closed in the magnetotail, Φ_N, varies largely independently of the solar wind conditions and as a result, F_{PC} is also variable.

The magnetospheric response to dayside driving can be measured in several related ways: the auroral response, the response of the current systems monitored using magnetometers, emission of radio waves, electric voltages, pulsations, and the rate of magnetospheric/ionospheric convection. The enhancements of

the eastward and westward electrojets is inferred from the intensification in the Auroral Upper (*AU*) and Auroral Lower (*AL*) indices [*Davis and Sugiura*, 1966]. *AU* and *AL* are computed by tracing out the upper and lower envelopes of overlaid measurements of the north-south magnetic deviations in the auroral zones [*Davis and Sugiura*, 1966].

The occurrence and rate of closure of flux on the nightside responds in distinct ways to the dayside driving. These are referred to as magnetospheric modes [*Henderson*, 2004; *Partamies et al.*, 2009; *Huang et al.*, 2009; *Pulkkinen et al.*, 2010; *Cai and Clauer*, 2013; *Walach and Milan*, 2015]. One of the most well-known modes is the substorm, which is often characterized by its auroral signatures: *Akasofu* [1964] found that a bright arc forms on the equatorward boundary of the nightside auroral oval, which explosively brightens and subsequently moves poleward. Prior to the explosive brightening of the auroral onset arc, the area enclosed by the auroral oval, the polar cap, expands equatorward, which is coincident with dominant dayside reconnection and is known as the growth phase of the substorm [e.g., *Coumans et al.*, 2007; *Baker et al.*, 1996, 1999; *McPherron*, 1970; *Milan et al.*, 2003]. The brightening which *Akasofu* [1964] observed has since become known as the onset of the substorm, which is closely followed by an explosive poleward expansion of the bulge as well as a sudden enhancement in *AL*, and a lesser enhancement in *AU*. This is known as the expansion phase and coincides with nightside reconnection dominating over dayside reconnection [e.g., *Baker et al.*, 1999; *Milan et al.*, 2003]. The expansion phase is followed by a recovery phase, which is characterized by a further, but less energetic contraction of the polar cap, a redistribution of flux, and a recovery of the electroject indices, *AU* and *AL* [e.g., *Elphinstone et al.*, 1996; *Milan et al.*, 2003].

Contrary to the dynamic substorm, periods of steady magnetospheric convection (SMC) are times when the magnetosphere is driven but does not undergo any of the substorm phases [*Pytte et al.*, 1978; *Sergeev et al.*, 1996; *O'Brien et al.*, 2002; *McPherron et al.*, 2005; *DeJong et al.*, 2009]. Instead, nightside and dayside reconnection rates are steady and roughly equal, such that they are also known as "balanced reconnection intervals" [*DeJong et al.*, 2009]. It is common for the magnetosphere to transition from a substorm to an SMC, as an intermediary phase between substorm expansion and recovery if the IMF B_Z remains southward for a prolonged period [*Walach and Milan*, 2015]. As the dayside and nightside reconnection rates are balanced during SMCs, the flows in the ionosphere and the polar cap flux are expected to stay constant [*McWilliams et al.*, 2008; *DeJong et al.*, 2009; *Walach and Milan*, 2015]. The SMC comes to an end as the dayside reconnection rate decreases, due to a northward turning of the IMF.

Sergeev et al. [2001] found that during SMCs, the auroral oval was wide at the nightside, covering ~12° of latitude, the plasma sheet was relatively thick, and the lobe flux was decreased with enhanced magnetic flux closure and multiple bursty earthward flows or bursty bulk flows occurring in the midtail. They further concluded that during SMCs, auroral streamers associated with both bursty bulk flows and narrow injections occurred [*Sergeev et al.*, 2001]. Their results imply that SMCs only occur when the pressure in the magnetotail is somewhat stable, such that efficient reconnection without explosive events like substorms occur. Though they have "steady" in their name, SMCs are only quasi-steady in nature: previous studies reported that pseudo-breakups, i.e., auroral brightenings which resemble auroral onset but do not include the expansion of a substorm, occur frequently during SMCs [e.g., *Sergeev et al.*, 2001; *DeJong and Clauer*, 2005, and references therein]. These pseudo-breakups could be responsible for keeping the magnetosphere in a quasi-steady convection state via reconnecting small amounts of open flux at a time [*DeJong and Clauer*, 2005; *Milan et al.*, 2006]. *Yang et al.* [2010] used the Rice Convection Model, a simulation of the Earth's magnetosphere, to study the dynamics in the magnetotail during an SMC. They found distinct features in the nightside near-Earth plasma sheet: in comparison to substorm growth phases, the magnetic field is more stretched close to the Earth and is more dipolar in the plasma sheet, the plasma pressure is lower in the tailward plasma sheet, and the plasma sheet is thicker and its inner edge is closer to the Earth. All these imply that the auroral zone is thicker, matching the results from *Sergeev et al.* [2001]. *Yang et al.* [2010] also deduce that in order for the pressure in the tail to stay balanced for prolonged amounts of time, i.e., during SMCs, a low entropy boundary forms in the magnetotail rather than balancing the pressure via small reconnection channels as *DeJong and Clauer* [2005] inferred.

Sawtooth events (SEs) are quasiperiodic events of unloading of open magnetic flux [*Borovsky et al.*, 1993; *Belian et al.*, 1995; *Cai et al.*, 2006a, 2006b; *Walach and Milan*, 2015], with periods of approximately 2–4 h [*Cai and Clauer*, 2009]. They were first observed as sawtooth-like oscillations in the particle fluxes at geostationary orbit, with sharp increases of particle fluxes (i.e., dispersionless injections) followed by gradual decreases.

SEs appear to be large, quasiperiodic substorms, but it is still unclear if the tail dynamics are governed by different physical processes. For example, *Henderson* [2004] showed that a previously well-studied substorm interval was in fact an SE, which raises the question of whether any physical distinction exists between the two magnetospheric modes.

Using the Assimilative Mapping of Ionospheric Electrodynamics Technique [*Richmond and Kamide*, 1988], *Cai et al.* [2006a] found that the ionospheric convection pattern during substorms and SEs is very similar, but sawtooth events are more intense and much more variable than substorms, in terms of their convection rates.

Cai et al. [2006b] used measurements of the magnetic tilt angle from the GOES satellite at geostationary orbit to show that the dipolarization seen during sawtooth events is very similar to that of substorms. They found that SEs are primarily initiated at the nightside between 22 and 0 MLT, and compared to substorms, the magnetotail is more stretched, prior to dipolarization onset. Subsequently, the SE's dipolarization expands both eastward and westward, similar to substorms; however, expansion occurs over a wider local time extent than substorms, but it is nevertheless constrained to the nightside.

Henderson et al. [2006] independently reached similar conclusions: The dipolarization which initiates the teeth starts at the nightside (in the dusk to midnight region) of the magnetosphere and then spreads further duskward and dawnward. They conclude that SEs can be considered as quasiperiodic substorms, but as the dayside reconnection rates are much larger than during substorms, a single dipolarization or substorm-like energy-unloading process is not enough to unload all the energy stored in the magnetotail, and as a result, we see the pulsing unloading events. A study by *Kavanagh et al.* [2007] looked at a series of sawteeth using riometer data, showing that three out of four teeth were consistent with the conjecture that sawteeth are recurring substorms.

Huang and Cai [2009] investigated the pressure in the magnetotail before and during SEs using measurements by the Geotail satellite. They found that the pressure is 3 times higher at SE onset than during quiet times and is dependent on solar wind parameters. This matches the findings by *Walach and Milan* [2015], who showed that the dayside reconnection rate just before SEs is on average 3 times as high as at substorm onset. Contrary to *Henderson et al.* [2006], this would suggest that rather than being different magnetospheric modes, SEs are simply large-scale successive substorms resulting from enhanced dayside reconnection. Along the same lines, *Hubert et al.* [2008] showed that sawtooth events take place when the magnetosphere is overloaded by open magnetic flux produced on the dayside at an exceptionally large rate.

In this study, we compare the auroral response to different modes of the magnetosphere (i.e., substorms, SMCs, and SEs) statistically using data from the Imager for Magnetopause-to-Aurora Global Exploration (IMAGE) far ultraviolet (FUV) instrument suite [*Mende et al.*, 2000a]. In the past, studies of the aurorae during SMCs and SEs have been focused on small data sets and case studies. For example, *Sergeev et al.* [1996] observed small-scale auroral activations during SMCs, including north-south aligned arcs and streamers. To this date though, no large statistical comparison of aurorae during different modes has been undertaken. This paper provides the first comprehensive statistical study of auroral oval configurations and dynamics during different magnetospheric modes to determine what the differences are.

2. Data

The IMAGE satellite was operational from June 2000 to October 2005 and gathered enough data such that the data set is suitable for large-scale studies. IMAGE was in a polar elliptical orbit, with apogee and perigee of 7 R_E and 1000 km, respectively, with an orbital period of ~13 h. In the months after launch, the apogee was over the Northern Hemisphere such that the northern aurorae could be observed with a cadence of ~2 min for ~10 continuous hours of every orbit [*Burch*, 2000; *Mende et al.*, 2000a]. Over the mission lifetime, the orbit precessed such that in 2003 both Northern and Southern Hemisphere aurorae could be glimpsed for short periods. However, by 2004 prolonged observations of the Southern Hemisphere aurorae could be made instead of observations of the northern aurorae.

In this study, we use data from the Wideband Imaging Camera (WIC) [*Mende et al.*, 2000b] and one of the Spectrographic Imagers (SI12) [*Mende et al.*, 2000c]. WIC observed 140–190 nm emission and is sensitive mainly to Lyman-Birge-Hopfield (LBH) N2 lines [*Mende et al.*, 2000a, 2000b]. Although a portion of this emission can be due to excitation by the secondary electrons produced by the proton aurora, detailed studies have shown

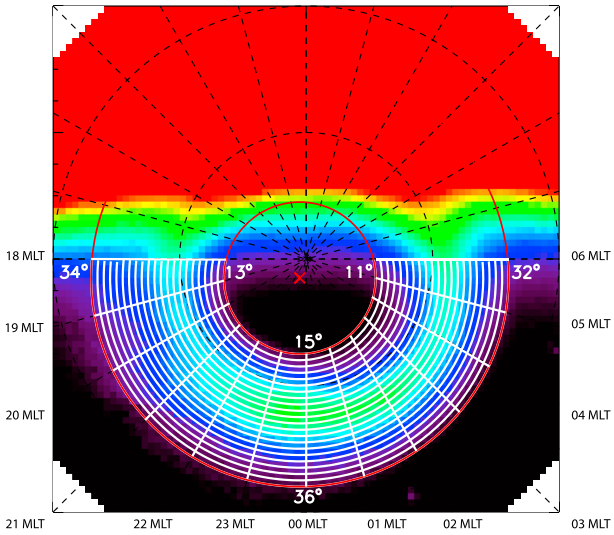

Figure 1. Schematic illustrating the data binning. The underlying image is an example of a WIC-averaged picture from the superposed epoch analysis for substorms. The dashed black dashed lines divide the MLT sectors and circles separated by 10° of geomagnetic latitude, centered on the geomagnetic North pole located at the center of the image. The red lines show the inner and outer boundary circles defined for the analysis in Figures 2, 4, and 3, which hold the majority of auroral power for all images. The inner and outer circles have radii of 12° and 33°, respectively. The center of these circles is shown by the red cross (centered on [−1°,−3°] with respect to the geomagnetic pole). The white lines indicate the bins selected for the latitudinal superposed epoch analysis (semicircles), separated by 1° of latitude and MLT bins (lines).

that WIC emission occurs primarily due to electron particle precipitation [e.g., *Gérard et al.*, 2001; *Hubert et al.*, 2001, 2002; *Coumans et al.*, 2002]. *Hubert et al.* [2001] report a ∼10–15% contribution on the nightside due to secondary electrons originating from the proton aurora and *Hubert et al.* [2002] show that this contribution is highest during the most quiet times. As we are considering periods where the magnetosphere is driven by dayside reconnection in this paper, we refer to the WIC emission as electron aurora throughout this paper. SI12 (121.8 nm) primarily observed Doppler-shifted Lyman-α emission from downward traveling charge exchanging protons or hydrogen atoms, we refer to this emission throughout the manuscript as proton aurora [*Mende et al.*, 2000c; *Gérard et al.*, 2001; *Coumans et al.*, 2002].

The study by *Walach and Milan* [2015] compared SMCs, substorms, and SEs in terms of their general magnetospheric dynamics. They looked at solar wind drivers and the magnetospheric response: *AU*, *AL*, *SYM-H*, F_{PC}, and auroral brightness. The polar cap flux was calculated from fitting ovals to the inner edge of the IMAGE data, which was assumed to approximate the open closed field line boundary [*Blanchard et al.*, 1995; *Boakes et al.*, 2008; *Shukhtina and Milan*, 2014]. The auroral brightness in the study by *Walach and Milan* [2015] was calculated from the maximum auroral emission by SI12 and WIC, as well as the total emission measured by SI12.

In this study, however, we will look at the nightside morphological auroral changes during different magnetospheric modes, highlighting the differences which may be the result due to varying physical processes occurring during each mode. For this comparative study, the event lists we use are identical to those employed by *Walach and Milan* [2015]: The substorm onsets were identified using IMAGE data by *Frey et al.* [2004], who looked for a clear local brightening of the aurora, as well as an expansion of the brightening to the poleward boundary of the auroral oval and an azimuthal spreading. The SEs were identified using undispersed dipolarization signatures of energetic protons and electrons at geosynchronous orbit by *Cai et al.* [2006a] and Henderson and McPherron [*Pulkkinen et al.*, 2007]. All substorms appearing in the Frey substorm list, which occurred within ±15 min of SE onset were removed from the substorm list by us. The initial SMC list was compiled by *Kissinger et al.* [2011] using the *AU* and *AL* indices as a proxy for convection. *Walach and Milan* [2015] used Φ_D, F_{PC}, and the auroral brightness to further remove events where no steady convection was occurring. The SMC list was then further subdivided to find those SMCs which followed a substorm onset in the preceding 2 h [*Walach and Milan*, 2015]. For the SMCs preceded by a substorm, the event start time is shifted to the corresponding substorm onset as was done in the previous study. These are SMCs which *Walach and Milan* [2015] identified as "driven substorm expansion and recovery phases." After these selection and elimination processes, 4083 substorms, 273 SEs, and 154 SMCs with preceding substorms were selected.

To compare the auroral imagery of the different event types, a superposed epoch analysis is performed. For each event type we create average images at 2 min cadence from 2 h before onset to 4 h after onset. WIC data are averaged onto a 80×80 grid by calculating the median for each pixel, where each grid cell is the equivalent of 1° of latitude to a side. For SI12 data, a 40 × 40 grid of 2° cells is used due to the lower resolution of the camera. The individual median images are included as supporting information in the form of animations.

To analyze the auroral dynamics in more detail, we then bin the pixels for each average image into 1 h MLT sectors of the nightside and latitudinal bands of 1° width. The individual bin sizes are shown by the white lines in the schematic of Figure 1. To mask the main parts of the aurora, two concentric circles were used as boundaries for the binning. These were chosen manually, with the center defined as [−1°, −3°], with respect to the geomagnetic pole. The smallest circle was chosen to have a radius of 12° and the outer boundary was chosen to have a radius of 33°. As the semicircles are shifted from the geomagnetic pole, the inner and outer radii are annotated in terms of geomagnetic colatitude near dusk, dawn, and midnight in Figure 1. We further omit the dayside in this analysis due to the presence of dayglow. To eliminate dayglow as much as possible, we only use WIC data from the winter months (spring equinox to autumn equinox) and subtract the 5% value from the bottom of all brightnesses from each image. The white semicircles shown in Figure 1 show the radial bins which we later use to explore any latitudinal movement of the oval as a whole. For the time evolution in the MLT bins shown later, we thus take the mean auroral brightness of each MLT bin, and to find the latitudinal evolution of the aurora, we calculate the mean for each longitudinal bin.

Figures 2–4 show the binned superposed epoch analyses of the IMAGE FUV SI12 and WIC data. Figures 2c, 3c, and 4c and Figures 2d, 3d, and 4d show the averaged pixels by MLT bins (SI12 and WIC, respectively) with respect to time from onset. Figures 2e, 3e, and 4e (SI12) and Figures 2f, 3f, and 4f (WIC) show the averaged latitudinal bins with respect to onset. Onset is marked by the dashed vertical line at $t = 0$. The bottom two rows of panels in Figures 2–4 show selected averaged images from the superposed epoch analysis from SI12 (top row) and WIC (bottom row). The selected individual images (bottom two rows) are taken from −60, 0, 20, 40, 60, and 120 min with respect to onset. The full variation of the superposed epoch analysis is included as supporting information in the form of animations (both WIC and SI12 for each event type). Figures 2a, 3a, and 4a show the brightness evolution of the MLT bins measured by SI12, with each MLT bin normalized to the preonset brightness (average across $t = -5$ min from onset to onset) and the same is shown for WIC in Figures 2b, 3b, and 4b. The grey contours in Figures 2a, 3a, and 4a and Figures 2b, 3b, and 4b indicate the boundary between brighter and dimmer aurora, in comparison to preonset brightness (i.e., the values at the contours are set to 1.1). This is instructive for studying the postonset brightenings, as the grey contours indicate when the auroral intensity returns to preonset levels in each MLT sector.

3. Results

We first discuss the results of the substorm analysis presented in Figure 2. Prior to onset, the auroral oval gradually expands equatorward to lower latitudes (see Figures 2e and 2f). Figures 2c and 2d, displaying the MLT-dependent behavior, show that in all nightside MLT sectors, both the electron and proton aurorae are dim prior to onset, with the proton emission being generally higher at dusk than at dawn. Nevertheless, the auroral oval never fully disappears (Figures 2e and 2f). In Figures 2e and 2f, in both the WIC and SI12 data, we see the oval confined to radial bins ∼18–25°, just before onset (i.e., the auroral oval is approximately 10–12° wide 5 min before onset). At onset, the aurora brightens between 22 and 0 MLT in the WIC data and between 22 and 1 MLT in the SI12 data (Figures 2a–2d). In the superposed epoch analysis, this brightening seems to occur over a few hours of MLT, but this is because auroral onset occurs in very confined locations, which vary and are therefore blurred in the averaging process. Latitudinally (see Figures 2e and 2f), the auroral oval also expands poleward and equatorward after onset, with the poleward expansion being more obvious. The brightening expands to cover a wider MLT extent, which we see primarily develop in the 10–40 min after onset (Figures 2a and 2b). The brightening in the electron aurora moves across the midnight meridian toward dawn after expansion, covering 18–06 MLT at $t = 40$ min, whereas the brightest proton aurora stays closer to midnight (20–04 MLT), relative to preonset brightness (Figures 2a and 2b). At $t = 100$ min, the auroral oval covers a latitudinal width of approximately 14–17°. The electron aurora starts to recover from the brightening and expansion after ∼60 min (Figure 2b), whereas the proton aurora takes almost twice as long (Figure 2a). After ∼130 min after onset, all proton brightness lies in the postmidnight sectors. For all MLT sectors to return to preonset brightness also takes less time for the electron aurora (less than ∼2 h) than the proton aurora (more than 4 h; cf. grey contours in Figures 2a and 2b).

For SEs, the superposed epoch analysis are plotted on a different color scale, as the aurora is overall much brighter, as also shown by *Walach and Milan* [2015]. The superposed epoch analysis of the radial bins reveals that the auroral oval for SEs also expands to lower latitudes prior to onset, but much more significantly. Unlike substorms, the auroras are already very bright before onset (Figures 3e and 3f) and cover a slightly wider latitudinal extent of approximately 12–14° 10 min before onset. At onset, the brightness seen in the proton

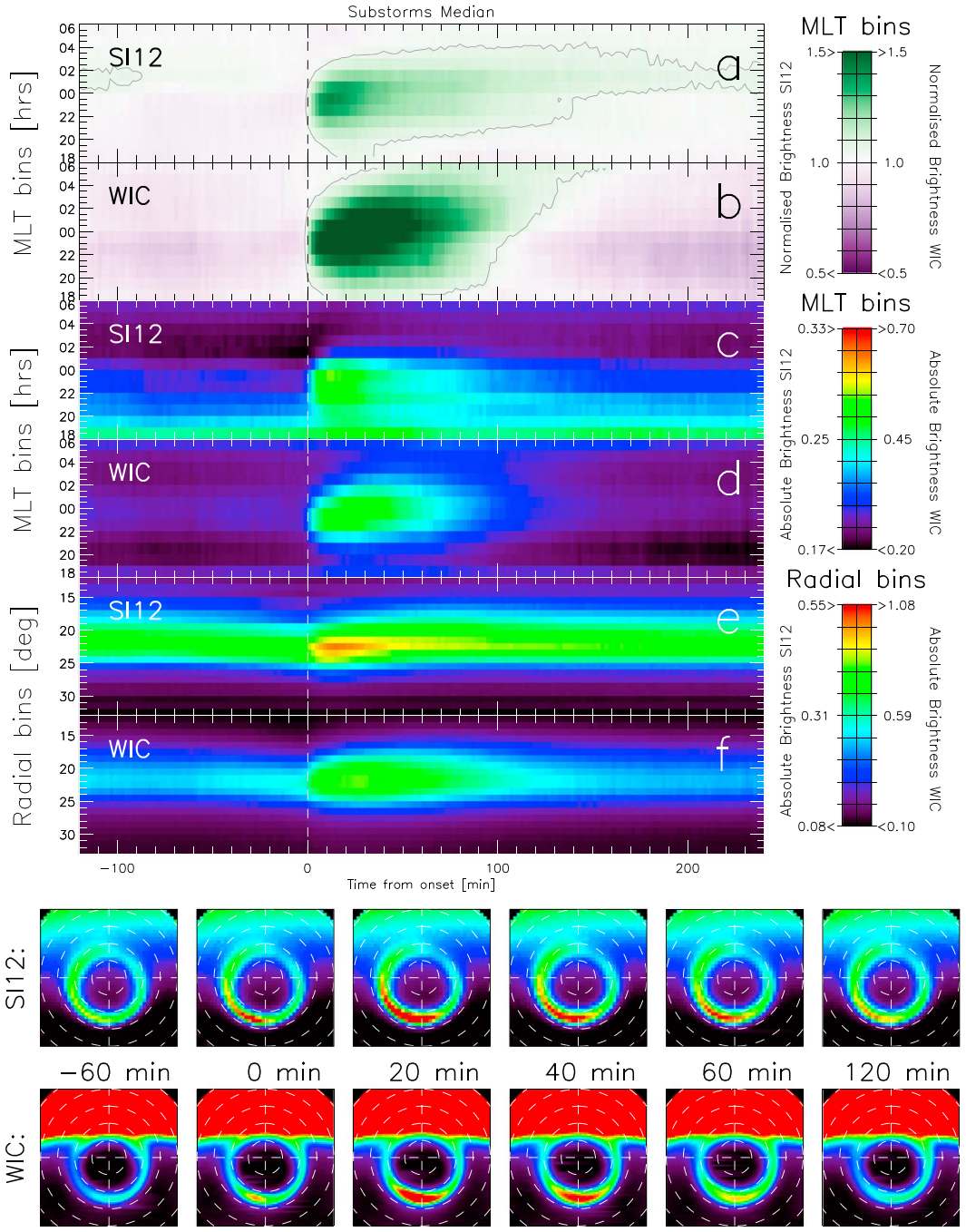

Figure 2. Superposed epoch analysis of substorms from IMAGE FUV SI12 and WIC data. Panels show the brightness across the nightside MLT bins, normalized by preonset brightness for (a) SI12 and (b) WIC, the absolute auroral brightness per MLT bin for (c) SI12 and (d) WIC and the auroral brightness per latitudinal bin for (e) SI12 and (f) WIC. The dashed line indicates substorm onset. The bottom two rows of panels show excerpts from the superposed epoch analysis of SI12 and WIC data at $t = -60$, 0, 20, 40, 60, and 120 min with respect to onset. All absolute brightnesses are in units of kR and the thumbnails have the same color scale as Figures 2e and 2f.

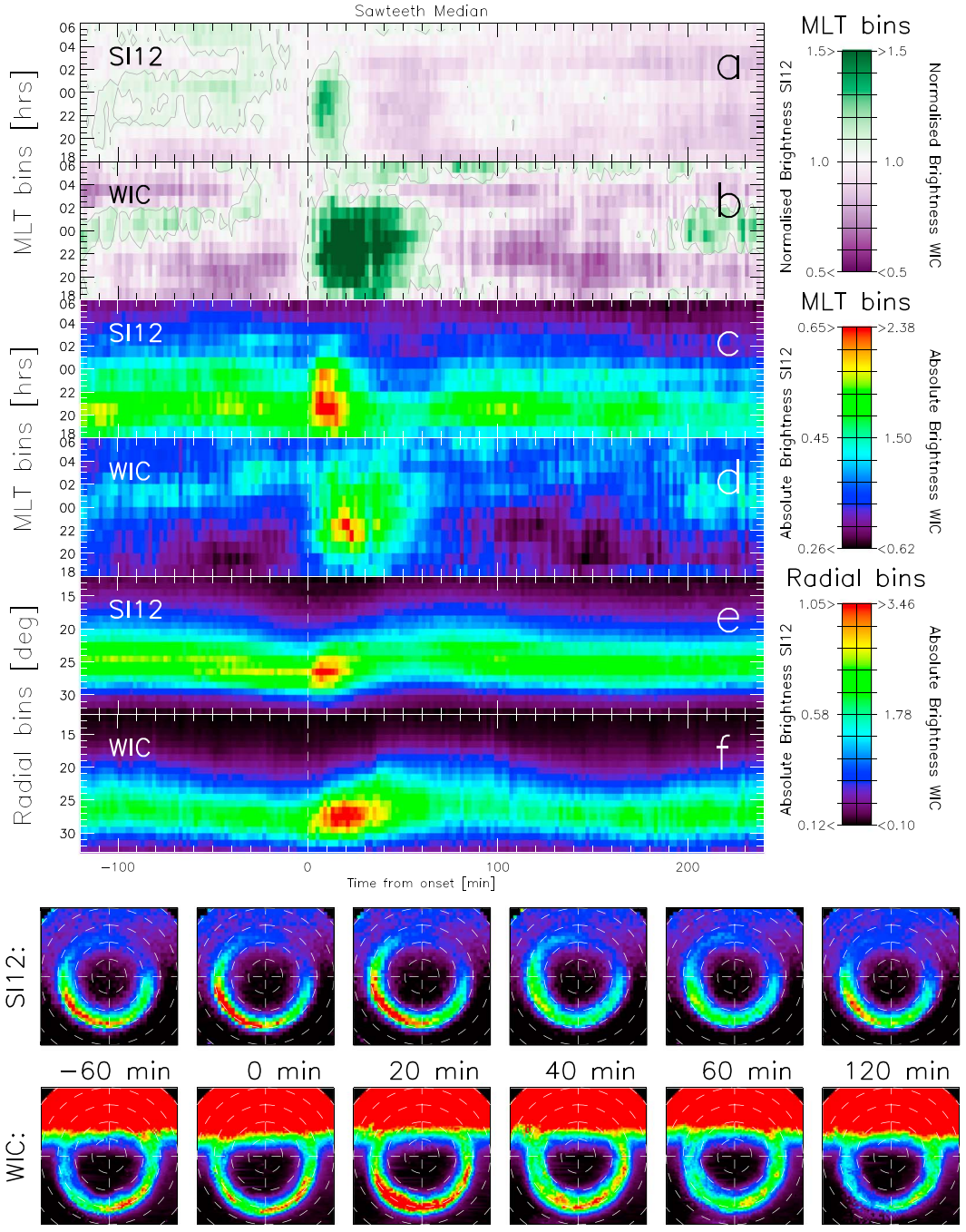

Figure 3. Superposed epoch analysis of sawtooth from IMAGE FUV SI12 and WIC data. Panels show the brightness across the nightside MLT bins, normalized by preonset brightness for (a) SI12 and (b) WIC, the absolute auroral brightness per MLT bin for (c) SI12 and (d) WIC and the auroral brightness per latitudinal bin for (e) SI12 and (f) WIC. The dashed line indicates sawtooth onset. The bottom two rows of panels show excerpts from the superposed epoch analysis of SI12 and WIC data at $t = -60$, 0, 20, 40, 60, and 120 min with respect to onset. All absolute brightnesses are in units of kR and the thumbnails have the same color scale as Figures 3e and 3f.

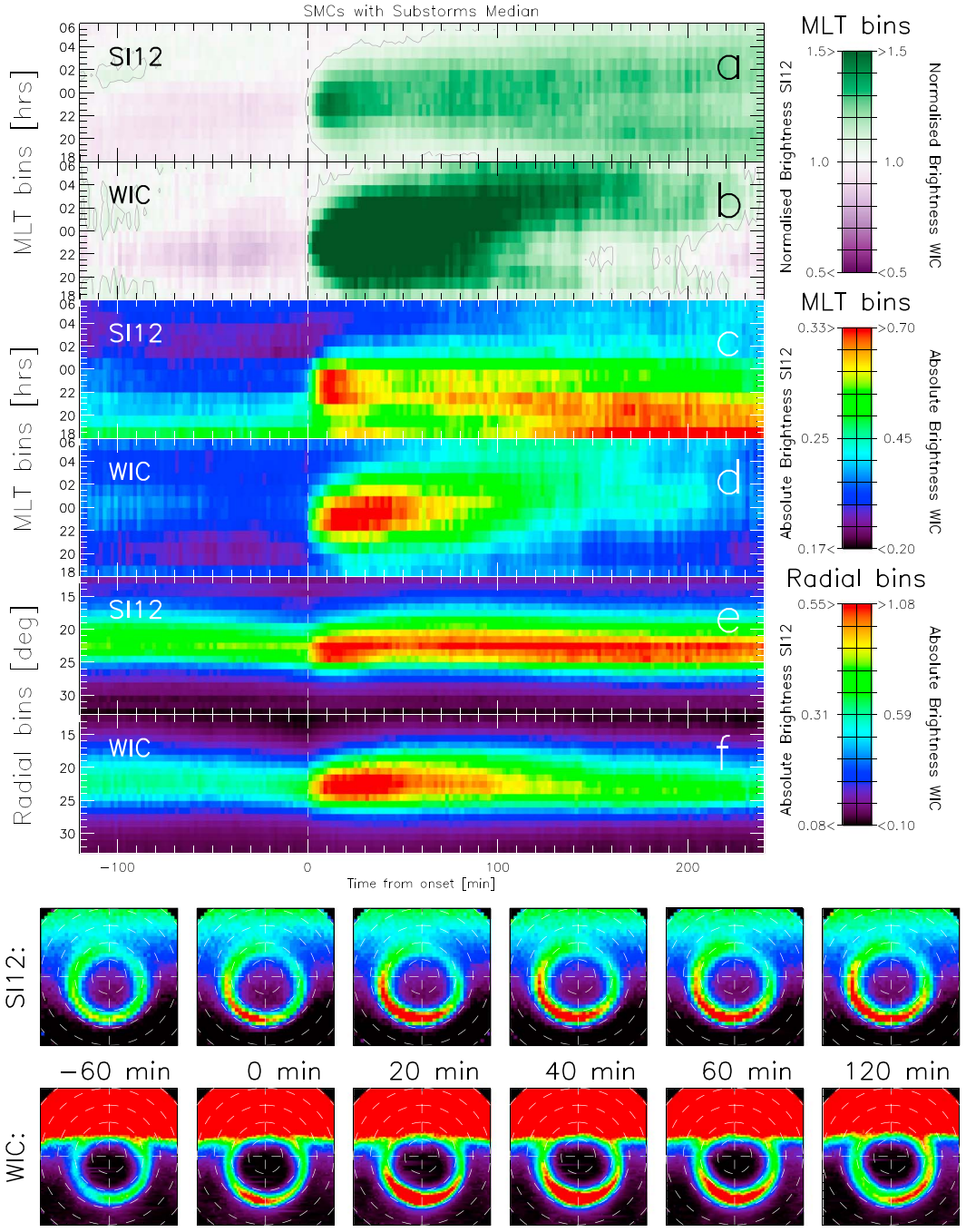

Figure 4. Superposed epoch analysis of SMCs with preceding substorms from IMAGE FUV SI12 and WIC data. Panels show the brightness across the nightside MLT bins, normalized by preonset brightness for (a) SI12 and (b) WIC, the absolute auroral brightness per MLT bin for (c) SI12 and (d) WIC and the auroral brightness per latitudinal bin for (e) SI12 and (f) WIC. The dashed line indicates substorm onset, which precede the SMCs. The bottom two rows of panels show excerpts from the superposed epoch analysis of SI12 and WIC data at $t = -60$, 0, 20, 40, 60, and 120 min with respect to onset. All absolute brightnesses are in units of kR and the thumbnails have the same color scale as Figures 4e and 4f.

aurora increases and it begins to move poleward, similar to the electron aurora; however, the electron aurora brightening occurs on a longer time scale of ~1 h. At $t = 60$ min, the auroral oval covers 15–16° in latitude. After the poleward contraction (~1 h after onset), the auroral oval then moves again to lower latitudes (Figures 3e and 3f), which is indicative of the conditions preceding the next tooth. Due to the slightly different timings of each tooth, any periodicity will be somewhat smoothed.

Before onset, the electron aurora is brightest in the early morning sectors (1–4 MLT) (Figure 3d). At onset a brightening occurs, which is centered at 21 MLT in the electron aurora (Figures 3b and 3d). This brightening then expands duskward and dawnward very rapidly and reaches its full MLT extent within approximately 10 min (Figures 3a and 3b). Within the time span of 10 min, all nightside sectors from 18 to 4 MLT see a brightening in the electron aurora. Coincidentally, the bright electron aurora also expands latitudinally, to cover a latitudinal band of over ~10°. This feature then continues to exist for approximately 1 h, after which the onset brightening in the electron aurora starts to fade and the MLT sectors from 18 to midnight become much less active in the WIC data. The proton aurorae behave differently to the electron aurora during SEs (Figure 3a). Longitudinally, the bright aurora prior to onset is spread out more, especially toward dusk, and does not change significantly at onset. This only shows in Figure 3c, but not in Figure 3a and is thus more of a general feature, as opposed to onset related. At onset, the proton aurorae brighten near midnight (Figure 3a). The brightening is confined to MLTs from 18 to 4 and is very short-lived. After 20 min postonset, the brightening in the proton aurora has dimmed to preonset brightness levels in all MLT sectors (see grey contour in Figure 3a), which is inherently shorter than the recovery time for substorms.

Similar to substorms, SMCs with preceding substorms are dim in all MLT sectors, except for the proton aurora on the duskside, which is bright throughout the considered period (Figures 4c and 4d) and show a more latitudinally confined auroral oval, prior to substorm onset (Figures 4e and 4f). At $t = -10$ min, the aurora covers a latitudinal extent of approximately 9–12°, which expands to 16–18° at $t = 60$ min. The brightening at onset is also extremely similar to substorms not preceding SMCs, but generally, the auroral oval is much brighter during these types of events and stays much brighter after the substorm expansion has occurred, especially in the SI12 data (cf. Figures 4a–4d). To facilitate comparison, the substorms and SMCs were plotted with the same color scale as substorms. Instead of the brightening in the MLT sectors returning to preonset brightness after ~100 min, as occurs after substorms, the electron brightening stays primarily dawnward (see Figure 4 b) at ~120 min postonset and stays bright for many hours, with the brightening strongest at 2 MLT. The proton aurora behaves very differently to substorms, as it covers a much wider MLT extent: Approximately 100 min after onset, it covers the whole nightside from 18 to 06 MLT. The proton aurora begins to dim slightly in the nightside MLT sectors around midnight at approximately the same time as the electron aurora and the bright proton aurora then mainly covers the dusk and dawn regions toward the end of the shown interval (during steady convection) rather than being centered around the midnight MLT sector, as it happens during the preceding substorm onset. During SMCs the bright aurora appears to cover not only a wider MLT extent but also, on average, a wider latitudinal range than substorms.

For substorms, the total average preonset auroral brightness across the nightside (from $t = -5$ min to $t = 0$ min; i.e., the total intensities which are used for the normalization) is 2.38 kR for SI12 and 3.24 kR for WIC; for SMCs with preceding substorms, these intensities are 2.59 kR for SI12 and 3.83 for WIC, and for the SEs these are 5.49 kR for SI12 and 11.82 kR for WIC. This shows that the proton aurora and electron aurora are on average over 2 or 3 times brighter preonset for sawtooth events in comparison to ordinary substorms.

4. Discussion

We have examined the average auroral evolution during substorms, SEs, and SMCs preceded by a substorm onset, which are also briefly summarized in Table 1. We now discuss the commonalities and differences in more detail and contrast the results with other works.

Prior to substorm onset, when dayside reconnection is dominant and nightside reconnection is thought to be minimal [*Walach and Milan*, 2015], we see a mild equatorward expansion of the aurora, which is more visible in the WIC data than in the SI12 data (Figures 2e and 2f). We suggest that this is a result of the WIC data being more sensitive to variations than the SI12 data in general.

At substorm onset the auroral oval brightens. The brightest segments of the SI12 and WIC emission are at first centered near 23 MLT, with the brightest SI12 emission being shifted slightly more toward dawn than

Table 1. A Table Comparing the Different Auroral Features

	Substorms	SMCs With Preceding Substorms	SEs
Before onset	Expansion of auroral oval to lower latitudes	Expansion of auroral oval to lower latitudes	Most obvious expansion of auroral oval to lower latitudes (~5–10°); aurora is already brighter than intensifications seen during substorms
Electron aurora	Dawn sector bias		Brightest in early morning sectors (01–04 MLT)
Electron aurora covers	~12° at 00 MLT at $t = -10$ min	~13° at midnight at $t = -10$ min	~12° at midnight at $t = -10$ min
Proton aurora	Brightest on the duskside		Largest equatorward movement; general duskward bias
Proton aurora covers	~10° at 00 MLT at $t = -10$ min	~10° at 00 MLT at $t = -10$ min	~14° at 00 MLT at $t = -10$ min
At onset	Brightening on the nightside	Brightening on the nightside	Brightening on the nightside
Electron aurora	Brightening centered around 23 MLT		Brightening centered at 21 MLT
Proton aurora	Brightening centered around 23 MLT	Brightening occurs near midnight	
After onset	Auroral emission rapidly spreads poleward and equatorward (over time span of ~20 min)	Brightening continues over larger latitudinal and longitudinal range than substorms	Auroral emission spreads poleward and equatorward (faster than during substorms)
Electron aurora	Spreads across midnight meridian toward dawn (18–06 MLT)	Intensification moves from 22–0 MLT to 02–06 MLT	Spreads duskward and dawnward to reach full extent (18–04 MLT) within 10 min
	Recovery starts after ~ 60 min postonset		Brightening lasts ~1 h
	Intensification has returned to preonset levels ~ 100 min after onset		Aurora moves equatorward after ~1 h
Electron aurora covers	~17° at 00 MLT at $t = 60$ min	~18° at 00 MLT at $t = 60$ min	~15° at 00 MLT at $t = 60$ min
Proton aurora	Stays closer to midnight (20–04 MLT)	Covers entire nightside	Brightening confined to MLTs from 18–04
	Recovery starts after ~120 min postonset	Brightening continues for hours after onset	20 min after onset the aurora has returned to preonset brightness levels in all MLT sectors
	After ~130 min after onset emission lies primarily in postmidnight sectors	Intensification moves to dusk and dawn sectors after ~120 min	Aurora moves equatorward after ~100 min
Proton aurora covers	~14° at 00 MLT at $t = 60$ min	~16° at 00 MLT at $t = 60$ min	~16° at 00 MLT at $t = 60$ min

the WIC emission (see individual thumbnails below panels in Figure 2). We postulate that this spatial divergence in brightenings is a manifestation of the substorm current wedge forming [*Kepko et al.*, 2015; *Milan et al.*, 2006]. In the traditional picture of the substorm current wedge, field-aligned currents will flow from the plasma sheet along the magnetic field lines into the inner magnetosphere. There they will flow westward and form the auroral electrojet. Further toward the west, the current will again flow along magnetic field lines and close with the tail currents. Different models of this substorm current wedge have since emerged (see *Kepko et al.* [2015], for a more complete discussion), including detailed observations, which indicate that the current wedge may actually consist of more than one "wedge" or multiple sheets of upward and downward field-aligned currents [e.g., *Forsyth et al.*, 2014; *Murphy et al.*, 2013]. As the brightest segments of the electron aurora at onset are shifted westward, compared to the proton aurora, we would expect there to be upward field-aligned currents flowing, which is analogous to the radial outward part of the current wedge toward the cross-tail current (by convention, downward flowing electrons are equivalent to an upward current). Where protons precipitate downward, on the other hand, electrons may move upward with respect to the protons, meaning a planetward field-aligned current will form. Thus, we think that these initial brightenings, at and just before substorm onset (see supporting information), are a statistical view of the substorm current wedge forming, as was also shown in a case study by *Milan et al.* [2006, Figure 7]. *Gérard et al.* [2004], however, studied onset latitudes of 78 individual substorms using IMAGE data and found no statistically significant difference in the locations of the proton and electron onsets.

After onset, the auroral oval retreats poleward, which is more rapid than the previous equatorward movement, the development of the substorm auroral bulge. This is unsurprising, as a previous superposed epoch analysis of the same events revealed that the polar cap flux, F_{PC}, shows a clear increase prior to onset and a decrease after onset for substorms [*Walach and Milan*, 2015]. *Mende et al.* [2003] also performed a superposed epoch analysis of SI12 and WIC data for substorms and although they binned the data with respect to local onset, they found that the polarward and equatorward auroral boundaries with respect to latitude trace out the same pattern that we see in Figures 2e and 2f. The main difference is that their traces are displaced equatorward by ∼10° of our bright aurora, which we attribute to their use of a smaller data set (91 substorms) and are thus likely to have missed many weak substorms, where the auroral oval is generally closer to the geomagnetic pole [*Milan et al.*, 2009]. Indeed, averaging the set of images results in a blurred image with auroral emissions likely to extend across a latitude range broader than any individual case.

At onset, both the proton and electron aurorae brighten explosively, which primarily occurs at 23 MLT, but can cover most nightside MLT sectors [*Frey et al.*, 2004; *Gérard et al.*, 2004; *Meng and Liou*, 2004; *Newell et al.*, 2001]. This brightening then spreads duskward and dawnward, extending across midnight from ∼18 to 4 MLT (SI12) and ∼18–6 MLT (WIC) 20 min after onset, which is when *AL* is on average the lowest during the substorm cycle [*Walach and Milan*, 2015]. We can see from Figures 2a and 2b, that in both cases the expansion of the brightening toward dusk occurs faster than the expansion toward dawn. Concurrent with the longitudinal spreading of bright aurora, the intensification of the aurora (especially the electron aurora) also spreads latitudinally. After this (∼1 h after onset), the proton aurora begins to dim with the electron aurora staying bright for another hour, before it begins to dim. As shown in the previous study [*Walach and Milan*, 2015], the majority of the brightening lasts for ∼1 h. Figures 2a and 2b reveal, however, that the brightening lasts much longer in the proton aurora, compared to the electron aurora. The electron aurora has almost dimmed back to preonset levels ∼3 h after onset in all MLT sectors. The brightening in the electron aurora lasts longest in the dawn sectors, with the brightening relaxing to preonset intensities ∼160 min after onset at 6 MLT. Compared to preonset levels, the proton aurora brightening at 2 MLT takes over 4 h to recover. In a statistical study, *Blockx et al.* [2005] found that, generally, the location of the brightest SI12 emission is a good locator for how stretched the magnetotail is. The prolonged brightening at 2 MLT thus implies that the magnetotail is stretched at this location, leading to pitch angle scattering of protons [*Sergeev et al.*, 1983].

These intensifications cannot be driven by particle acceleration due to reconnection, as we see no particular electron brightenings in these MLT sectors. As such, we postulate that the majority of protons, which create these aurora, are drifting on closed field lines and as they enter a still stretched tail region, they will pitch angle scatter and create the aurora.

Mende et al. [2003] further find that "as the substorm expansion proceeds poleward, the electron precipitation remains relatively constant, while the protons fade because less energy is available from dipolarization. Thus, in the early phases we see the proton precipitation expanding with the surge electrons and in later phases

they do not seem to be present in the leading edge of the substorm surge." While this makes physical sense, it is not something we find. Although the electron precipitation is stronger, compared to preonset levels, the proton precipitation is the one we find to be more persistent after onset, even though it appears to start fading first. This is particularly obvious when comparing Figures 2a and 2b. We speculate that this is due to how the data were binned and could be alleviated by binning the data relative to substorm onset location, as was, for example, done by *Mende et al.* [2003]. The main purpose of this study is to compare the auroral distributions of the different magnetospheric response modes and while most substorms have a clearly defined onset location, SMCs do not and SEs can cover a large range of MLTs.

Sawtooth events appear to be quasiperiodic substorms, which occur during geomagnetic storms, when the solar wind driving of the magnetosphere is very high [*Walach and Milan*, 2015]. Unsurprisingly, the superposed epoch analysis of SEs (Figure 3) looks very similar to substorms prior to onset, as the auroral oval moves equatorward. At onset the electron aurora (WIC) brightens explosively near local midnight and then expands very rapidly duskward and dawnward (which agrees with *Cai et al.* [2006b] and *Henderson et al.* [2006]) while retreating toward the pole. *Mende et al.* [2003] find that the auroral oval moves equatorward, prior to substorm onset, but only by a marginal ∼1–2°. Our superposed epoch analysis reveals the same growth phase characteristic for substorms, but for sawtooth events; this auroral expansion prior to onset is larger (∼5–10° of latitude for WIC and ∼2–3° of latitude for SI12 data). This is due to the elevated levels of dayside reconnection during these events [*Walach and Milan*, 2015].

On average, we find that SI12 precipitation is higher in the range of 18–00 MLT than 00–06 MLT, indicating that injected protons drift westward from midnight, but as Figures 3a and 3b do not show this feature, it is unrelated to event onset. Prior to SE onset, the SI12 aurora clearly moves to much lower latitudes than it ever sits at during the other types of events, and the magnetotail must be much more stretched during those periods than during ordinary substorms. This fits the previous results from *Walach and Milan* [2015], where we showed that the solar wind driving is ∼3 times as large during SEs than during substorms and as a result, F_{PC} is also much higher. The brightening we see at SE onset occurs between 20 and 00 MLT, similar to substorms. This confirms the results of *Cai et al.* [2006b] who showed that SEs are primarily initiated between 22 and 0 MLT. *Cai et al.*, 2006b further find that prior to SEs the magnetotail is more stretched, in comparison to substorms, which we can also confirm, as the SI12 emission is higher leading up to the SEs. We can also confirm their further result that the longitudinal expansion is similar to substorms, and although it happens faster for SEs, we do not see it occurring over a wider local time extent, as postulated by *Cai et al.* [2006b].

Also similar to substorms, we see a brightening at onset in the radial bins, in the SI12 data, but it is only a marginal increase in brightness. Similarly, *Walach and Milan* [2015] found that the total brightness seen in the SI12 emission only increases slightly at SE onset. This implies that many protons are pitch angle scattered into the atmosphere, and as such, the pressure on the central plasma sheet in the magnetotail is very high prior to onset due to there being a significant amount of open flux prior to the onset of an SE. As we have considered each tooth of a series of sawteeth as its own event, although faint, we see the beginning of the following tooth in Figure 3 at approximately 120 min, where the auroral oval moves poleward again.

Henderson et al. [2006] observe a double auroral oval configuration just before SE onset or between teeth. This is a feature, which we are unable to distinguish due to the averaging process.

It is important to note that for SEs there is a duskward bias of auroral emission seen by SI12 and a weaker, but still noticeable, dawnward bias of WIC emission, as also found by *Milan et al.* [2010]. After being injected into the inner magnetosphere via nightside reconnection, the electrons will drift eastward and the ions will drift westward, which is why the bright SI12 and WIC aurora move duskward and dawnward, respectively, after reconnection [*Gussenhoven et al.*, 1987; *Milan et al.*, 2009]. Other than the general dawn-dusk asymmetry in WIC and SI12 emission, we also see an expansion of the brightening in the MLT sectors, which resembles the brightening after substorms. The MLT expansion of the brightening after onset takes ∼10 min to reach its full extent for SEs, whereas for substorms this takes approximately twice as long. As shown by *Walach and Milan* [2015], the reconnection rate, as well as the overall auroral brightness and thus energy input into the inner magnetosphere are approximately twice as high near SE onset as for substorms, meaning that the azimuthal spreading of the brightening at onset is directly related to these quantities.

In general, as well as during the substorms and SEs, we find that the electron aurora appear to be more prevalent in the dawn sector than elsewhere. We postulate that this is due to electrons drifting generally eastward

in the magnetosphere on closed field lines. However, this does not explain why the duskward expansion after onset is faster than the dawnward expansion and why we do not see a similarly prominent feature in the proton aurora. We postulate that the faster westward expansion of the onset brightenings are due to the westward traveling surge observed during substorms [*Akasofu*, 1964], whereas the eastward drift of the bright WIC aurora after onset is related to injected electrons drifting eastward and eventually scattering in the ionosphere to produce aurora. While we see a similar feature in the panels showing the absolute proton brightness, it does not appear in the normalized brightness panels (Figures 3a and 3b). We speculate that this is due to the protons being less likely to enter the loss cone once they are on closed, nonstretched field lines (i.e., once they are on field lines which have undergone nightside reconnection and the initial particle injection has occurred). This may indicate that the loss cone refills due to wave-particle interactions or another process causing pitch angle scattering.

As the injected electrons drift eastward, the reconnection *X* line in the tail must thus expand eastward and westward in the 20 min after onset to cover the nightside from ~18 to 04 MLT. After ~100 min, the electron and proton aurorae start to dim, suggesting the end of a near-Earth neutral line (NENL) [e.g., *Baker et al.*, 1996], followed by a clear eastward drift of injected electrons.

The main difference between SEs and substorms is that, although the energy input into the magnetosphere is much higher during SEs due to enhanced reconnection rates [*Walach and Milan*, 2015; *Hubert et al.*, 2008], the onset related brightening takes less time to dim to preonset levels than for substorms (~20 min for the proton aurora, as opposed to over an hour postsubstorm). This means that there is a nonlinear relationship between the energy input and the recovery time of the system, which is a novel result.

In comparison to the substorms, the SMCs with preceding substorms show very similar signatures prior to and at onset. This is no surprise, as the SMCs' onsets were shifted to match the preceding substorm onset [*Walach and Milan*, 2015]. The main differences between substorms and these SMCs are seen after the substorm preceding the SMC has developed, especially in the proton aurora. Whereas usually, substorms start to decrease in auroral brightness ~20 min after onset, these substorms continue to produce bright aurora and are much brighter in general, seen by both WIC and SI12. This is due to the event being a driven expansion phase: *Walach and Milan* [2015] revealed that substorms end as both dayside and nightside reconnection rates reach very low levels, whereas for SMCs, both dayside and nightside reconnection rates continue to be elevated. As the magnetospheric system continues to be driven by reconnection, plasma is circulated around the magnetosphere. Seemingly, the magnetotail reaches a state where it is stretched, but reconnection can occur, as the SMC itself implies reconnection to take place, while the proton aurora continues to be bright for hours after the SMC-preceding substorms.

Whereas during substorm onset a localized (temporal and spatial) brightening is seen, the auroral brightenings seen during SMCs (after the substorms have subsided) are much less confined. Latitudinally, the bright aurora during SMCs cover a larger extent than during substorms, as also observed by *Sergeev et al.* [2001] and *Yang et al.* [2010]. In the MLT sectors, the SI12 aurora spreads across the nightside, with a slight dimming around midnight later on. WIC shows more variability across the MLT sectors: after the expansion phase of the substorm, the brightest MLT sectors on the nightside move from being at 22–0 MLT to 2-6 MLT, but after this, the WIC intensity continues to be enhanced across the nightside (Figure 4b), which we interpret to be the result of continued dayside driving and multiple injections. At ~120–150 min after substorm onset, a reconfiguration occurs where the aurora near midnight dims, but brightens in the dusk and dawn sectors (Figures 4a and 4b). This has implications for the magnetotail structure, as it implies an asymmetry in the location of its stretching. The electrons are primarily associated with reconnection, meaning the magnetotail reconnection site during SMCs has shifted toward dawn, whereas during substorms, it is primarily located near 23 MLT. The fact that we see bright proton aurora in both the dusk and dawn sectors means that the magnetotail is generally stretched.

This time scale of ~120–150 min itself is very interesting: It is approximately the duration of the substorm repetition rate (similar time scales were found by *Borovsky et al.* [1993] and *Newell and Gjerloev* [2011]), but even when the magnetosphere continues to be driven, there appears to be a marked change at ~120–150 min. This is obviously a characteristic time scale in the evolution of the tail in response to the onset of nightside reconnection. This break in the time scale can also be seen in the superposed epoch analysis of the SMCs with preceding substorms in Figure 3 of *Walach and Milan* [2015]. The question of what sets this time scale remains open, but we speculate that after the SMC-preceding substorm's expansion phase, the reconnection *X* line

(the NENL) moves tailward to form a distant neutral line (DNL) and reconnection continues in the more distant tail. The 120 min could be the typical time scale taken by a distant neutral line to form. Furthermore, the poleward edge of the aurora does not brighten or move rapidly during SMCs, which also indicates that the tail is stretched, but not stretched enough for a near-Earth neutral line to form.

The electron aurora behavior is thus overall very similar for substorms and SMCs, but much more prolonged for SMCs, whereas for the protons, the auroral behavior is very different.

In the past a double auroral oval has been observed during steady convection intervals [*Sergeev et al.*, 2001; *McWilliams et al.*, 2006], but we cannot say how persistent this feature is, as a double oval would be smeared out in the averaging process.

In general, substorms have been studied in great detail in the past, so the persistence of the related auroral features is well known, but many features found for the SEs and SMCs events remain to be tested for persistence.

5. Concluding Remarks

In this study we use data from the IMAGE SI12 and WIC instruments to produce superposed epoch analyses of the nightside aurora to compare substorms, sawtooth events, and steady magnetospheric convection events with preceding substorms. The data was binned latitudinally and by nightside MLT sectors, to resolve general auroral patterns in the electron and proton emission.

The analysis confirms the well-known behavior of the aurorae during substorms:

1. Prior to substorm onset, we see a general equatorward movement and thinning of the auroral oval, both of which are more pronounced in the electron aurora than the proton aurora.
2. At substorm onset, the aurorae brighten explosively, which occurs primarily near 23 MLT.
3. The most intense parts of the initial brightening of the electron and proton aurorae are shifted slightly in MLT, which we interpret to be an observation of the substorm current wedge.
4. The aurorae then expand poleward and the bright emission spreads duskward and dawnward from onset location, with the duskward spreading being approximately twice as fast as the dawnward spreading, a feature thought to be related to the westward traveling surge.
5. Approximately 20 min after onset, the bright proton aurorae cover the nightside from 18 to 4 MLT and the bright electron aurorae cover primarily 18–6 MLT.
6. After ~100 min after onset, the aurorae decrease in brightness, with the brightening in the proton aurorae being much more persistent (lasting for several more hours).

In addition to these well-studied features, we also observe the substorm current wedge, but this disappears after onset as the aurora becomes more dynamic and the detail is lost in the averaging process.

Prior to SE onset, the aurora moves equatorward, similar to substorms. At onset, the WIC emission brightens near local midnight and then expands duskward and dawnward. The brightenings over the nightside MLT sectors are also distributed similarly to substorms, but the aurorae are much brighter. We speculate that this is due to a more stretched tail, driven by the higher dayside reconnection rate.

As a result of the enhanced reconnection-related driving during and before SEs, both the proton and electron aurorae are much brighter. Nevertheless, the onset-related brightening is much shorter lived than the substorm and SMC-related brightenings. In fact, the time taken for the aurora to recover from an SE injection is approximately half that taken by substorms. This suggests that the relationship between the auroral recovery time after onset and energy input is nonlinear, suggesting that the auroral recovery time is controlled by another parameter.

The SMCs with preceding substorms start out in the same way as the substorms, but instead of dimming after ~20 min postonset, the auroral emission continues to be high in the SI12 and WIC, indicating that nightside reconnection continues and the tail is stretched. *Sergeev et al.* [1990, 1996] indicate that during SMCs, the tail configuration is intermediate between the substorm expansion and recovery phase. This specific configuration may be characterized by specific time scales. Approximately 100 min after onset, the proton brightening covers the whole nightside and we subsequently see a change from the substorm-like recovery: The proton brightenings continue to cover the nightside, with slightly increased brightenings in the dusk and dawn sectors. The brightest electron aurorae move from primarily covering 22–0 MLT to covering 03–06 MLT,

followed by a dimming after approximately 150 min postonset and a latitudinal narrowing of the WIC aurora. We interpret this break in behavior from 100 min postonset onward as a migration of the NENL toward a DNL.

In summary, we find the following:

1. The electron and proton aurora around SE onset appear like an energetic substorm onset, but the brightening after onset spans over a larger MLT extent, as they involve a larger amount of magnetic flux throughput and thus the nightside reconnection site must be wider.
2. Whereas the proton aurora during substorms takes over 2 h to fade back to a dim aurora, during SEs this process takes less than 1 h, despite the ongoing dayside and nightside reconnection.
3. Auroral signatures during SMCs with preceding substorms appear like substorms, but despite continued dayside driving of the system, we see a break in the nightside auroral activity, which reactivates 150 min after onset.
4. SMCs in general display brighter auroral emission than substorms as a result of continued dayside driving but covering a larger latitudinal and longitudinal range.
5. The latitudinal expansion and contraction of the auroral oval as a whole moves on similar time scales during substorms, SMC-preceding substorms, and SEs, despite different levels of dayside driving.

Acknowledgments

We thank the PI of IMAGE, J.L. Burch and the PI of FUV, S.B. Mende for the original IMAGE data set. M.-T.W. was supported by a studentship from the Science and Technology Facilities Council, UK. S.E.M. and J.A.C. were supported on the STFC grant ST/K001000/1 and ST/N000749/1. K.M. is partly funded by a Natural Sciences and Engineering Research Council of Canada Postdoctoral Fellowship. B.H. is supported by the FRS-FNRS. A.G. is supported by the STFC grant STM001059/1 and NERC grant NE/P001556/1. The original IMAGE data are available through the IMAGE FUV homepage (http://sprg.ssl.berkeley.edu/image/). The code used to generate the plots in this paper are stored in University of Leicester computers and are available on request.

References

Akasofu, S.-I. (1964), The development of the auroral substorm, *Planet. Space Sci.*, *12*, 273–282.

Baker, D. N., T. I. Pulkkinen, V. Angelopoulos, W. Baumjohann, and R. L. McPherron (1996), Neutral line model of substorms: Past results and present view, *J. Geophys. Res.*, *101*, 12,975–13,010.

Baker, D. N., T. I. Pulkkinen, J. Buechner, and A. J. Klimas (1999), Substorms: A global instability of the magnetosphere-ionosphere system, *J. Geophys. Res.*, *104*, 601–614.

Belian, R. D., T. E. Cayton, and G. D. Reeves (1995), Quasi-periodic global substorm generated flux variations observed at geosynchronous orbit, in *Space Plasmas: Coupling Between Small and Medium Scale Processes, Geophys. Monogr. Ser.*, vol. 86, edited by M. Ashour-Abdalla, T. Chang, and P. Dusenbery, p. 143, AGU, Washington, D. C., doi:10.1029/GM086p0143.

Blanchard, G. T., L. R. Lyons, J. C. Samson, and F. J. Rich (1995), Locating the polar cap boundary from observations of 6300 Å auroral emission, *J. Geophys. Res.*, *100*(A5), 7855–7862, doi:10.1029/94JA02631.

Blockx, C., J. C. Gérard, M. Meurant, B. Hubert, and V. Coumans (2005), Far ultraviolet remote sensing of the isotropy boundary and magnetotail stretching, *J. Geophys. Res.*, *110*, A11215, doi:10.1029/2005JA011103.

Boakes, P. D., S. E. Milan, G. A. Abel, M. P. Freeman, G. Chisham, B. Hubert, and T. Sotirelis (2008), On the use of IMAGE FUV for estimating the latitude of the open/closed magnetic field line boundary in the ionosphere, *Ann. Geophys.*, *26*(9), 2759–2769, doi:10.5194/angeo-26-2759-2008.

Borovsky, J. E., R. J. Nemzek, and R. D. Belian (1993), The occurrence rate of magnetospheric-substorm onsets: Random and periodic substorms, *J. Geophys. Res.*, *98*, 3807–3813.

Burch, J. L. (2000), IMAGE mission overview, *Space Sci. Rev.*, *91*, 1–14.

Caan, M. N., R. L. McPherron, and C. T. Russell (1977), Characteristics of the association between the interplanetary magnetic field and substorms, *J. Geophys. Res.*, *82*(29), 4837–4842, doi:10.1029/JA082i029p04837.

Cai, X., and C. R. Clauer (2009), Investigation of the period of sawtooth events, *J. Geophys. Res.*, *114*, A06201, doi:10.1029/2008JA013764.

Cai, X., and C. R. Clauer (2013), Magnetospheric sawtooth events during the solar cycle 23, *J. Geophys. Res. Space Physics*, *118*(10), 6378–6388, doi:10.1002/2013JA018819.

Cai, X., C. R. Clauer, and A. J. Ridley (2006a), Statistical analysis of ionospheric potential patterns for isolated substorms and sawtooth events, *Ann. Geophys.*, *24*, 1977–1991.

Cai, X., M. G. Henderson, and C. R. Clauer (2006b), A statistical study of magnetic dipolarization for sawtooth events and isolated substorms at geosynchronous orbit with GOES data, *Ann. Geophys.*, *24*, 3481–3490, doi:10.5194/angeo-24-3481-2006.

Coumans, V., J.-C. Gérard, B. Hubert, and D. S. Evans (2002), Electron and proton excitation of the FUV aurora: Simultaneous IMAGE and NOAA observations, *J. Geophys. Res.*, *107*(A11), 1347, doi:10.1029/2001JA009233.

Coumans, V., C. Blockx, J.-C. Gérard, B. Hubert, and M. Connors (2007), Global morphology of substorm growth phases observed by the IMAGE-SI12 imager, *J. Geophys. Res.*, *112*, A11211, doi:10.1029/2007JA012329.

Cowley, S. W. H., and M. Lockwood (1992), Excitation and decay of solar wind-driven flows in the magnetosphere-ionophere system, *Ann. Geophys.*, *10*, 103–115.

Cowley, S. W. H., and M. Lockwood (1996), Time-dependent flows in the coupled solar wind-magnetosphere-ionosphere system, *Adv. Space Res.*, *18*(8), 141–150, doi:10.1016/0273-1177(95)00972-8.

Davis, T. N., and M. Sugiura (1966), Auroral electrojet activity index *AE* and its universal time variations, *J. Geophys. Res.*, *71*(3), 785–801.

DeJong, A. D., and C. R. Clauer (2005), Polar UVI images to study steady magnetospheric convection events: Initial results, *Geophys. Res. Lett.*, *32*, L24101, doi:10.1029/2005GL024498.

DeJong, A. D., A. J. Ridley, X. Cai, and C. R. Clauer (2009), A statistical study of BRIs (SMCs), isolated substorms, and individual sawtooth injections, *J. Geophys. Res.*, *114*, A08215, doi:10.1029/2008JA013870.

Dungey, J. W. (1961), Interplanetary magnetic field and the auroral zones, *Phys. Rev. Lett.*, *6*(2), 47–48, doi:10.1103/PhysRevLett.6.47.

Dungey, J. W. (1963), Interactions of solar plasma with the geomagnetic field, *Planet. Space Sci.*, *10*, 223–237.

Elphinstone, R. D., J. S. Murphree, and L. L. Cogger (1996), What is a global auroral substorm?, *Rev. Geophys.*, *34*(96), 169–232, doi:10.1029/96RG00483.

Forsyth, C., et al. (2014), In situ spatiotemporal measurements of the detailed azimuthal substructure of the substorm current wedge, *J. Geophys. Res. Space Physics*, *119*, 927–946, doi:10.1002/2013JA019302.

Frey, H. U., S. B. Mende, V. Angelopoulos, and E. F. Donovan (2004), Substorm onset observations by IMAGE-FUV, *J. Geophys. Res.*, *109*, A10304, doi:10.1029/2004JA010607.

Gérard, J.-C., et al. (2001), Observation of the proton aurora with IMAGE FUV imager and simultaneous ion flux in situ measurements, *J. Geophys. Res.*, *106*(A12), 28,939–28,948, doi:10.1029/2001JA900119.
Gérard, J.-C., B. Hubert, A. Grard, M. Meurant, and S. B. Mende (2004), Solar wind control of auroral substorm onset locations observed with the IMAGE-FUV imagers, *J. Geophys. Res.*, *109*, A03208, doi:10.1029/2003JA010129.
Gussenhoven, M. S., D. A. Hardy, and N. Heinemann (1987), The equatorward boundary of auroral ion precipitation, *J. Geophys. Res.*, *92*(A4), 3273–3283, doi:10.1029/JA092iA04p03273.
Henderson, M. G. (2004), The May 23, 1986 CDAW-9C interval: A sawtooth event, *Geophys. Res. Lett.*, *31*, L11804, doi:10.1029/2004GL019941.
Henderson, M. G., G. D. Reeves, R. Skoug, M. F. Thomsen, M. H. Denton, S. B. Mende, T. J. Immel, P. C. Brandt, and H. J. Singer (2006), Magnetospheric and auroral activity during the 18 April 2002 sawtooth event, *J. Geophys. Res.*, *111*, A01S90, doi:10.1029/2005JA011111.
Huang, C.-S., and X. Cai (2009), Magnetotail total pressure and lobe magnetic field at onsets of sawtooth events and their relation to the solar wind, *J. Geophys. Res.*, *114*, A04204, doi:10.1029/2008JA013807.
Huang, C.-S., A. D. DeJong, and X. Cai (2009), Magnetic flux in the magnetotail and polar cap during sawteeth, isolated substorms, and steady magnetospheric convection events, *J. Geophys. Res.*, *114*, A07202, doi:10.1029/2009JA014232.
Hubert, B., J.-C. Gérard, D. V. Bisikalo, V. I. Shematovich, and S. C. Solomon (2001), The role of proton precipitation in the excitation of auroral FUV emissions, *J. Geophys. Res.*, *106*(A10), 21,475–21,494, doi:10.1029/2000JA000288.
Hubert, B., J.-C. Gérard, D. S. Evans, M. Meurant, S. B. Mende, H. U. Frey, and T. J. Immel (2002), Total electron and proton energy input during auroral substorms: Remote sensing with IMAGE-FUV, *J. Geophys. Res.*, *107*(A8), 1183, doi:10.1029/2001JA009229.
Hubert, B., S. E. Milan, A. Grocott, S. W. H. Cowley, and J. C. Gérard (2008), Open magnetic flux and magnetic flux closure during sawtooth events, *Geophys. Res. Lett.*, *35*, L23301, doi:10.1029/2008GL036374.
Kavanagh, A. J., G. Lu, E. F. Donovan, G. D. Reeves, F. Honary, J. Manninen, and T. J. Immel (2007), Energetic electron precipitation during sawtooth injections, *Ann. Geophys.*, *25*, 1199–1214, doi:10.5194/angeo-25-1199-2007.
Kepko, L., R. L. McPherron, O. Amm, S. Apatenkov, W. Baumjohann, J. Birn, M. Lester, R. Nakamura, T. I. Pulkkinen, and V. Sergeev (2015), Substorm current wedge revisited, *Space Sci. Rev.*, *190*, 1–46, doi:10.1007/s11214-014-0124-9.
Kissinger, J. E., R. L. McPherron, T.-S. Hsu, and V. Angelopoulos (2011), Steady magnetospheric convection and stream interfaces: Relationship over a solar cycle, *J. Geophys. Res.*, *116*, A00I19, doi:10.1029/2010JA015763.
Lockwood, M., and S. W. H. Cowley (1992), Ionospheric convection and the substorm cycle, in *Proceedings of the First International Conference on Substorms (ICS-I)*, pp. 99–109, European Space Agency Publ. ESA SP-335, Nordvijk, Netherlands.
McPherron, R. L. (1970), Growth phase of magnetospheric substorms, *J. Geophys. Res.*, *75*(28), 5592–5599, doi:10.1029/JA075i028p05592.
McPherron, R. L., T. P. O'Brien, and S. Thompson (2005), Solar wind drivers for steady magnetospheric convection, in *Multiscale Coupling of Sun-Earth Processes*, edited by A. T. Y. Lui, Y. Kamide, and G. Consolini, pp. 113–124, Elsevier Science, Amsterdam, doi:10.1016/B978-044451881-1/50009-5. [Available at http://www.sciencedirect.com/science/article/pii/B9780444518811500095.]
McWilliams, K. A., J. B. Pfeifer, R. L. McPherron, and H. U. Frey (2006), SuperDARN and IMAGE WIC observations during intervals of steady magnetospheric convection, in *International Conference on Substorms-8*, pp. 175–180, Dept. Physics, Univ. of Alberta, Banff, Alberta, C. A.
McWilliams, K. A., J. B. Pfeifer, and R. L. McPherron (2008), Steady magnetospheric convection selection criteria: Implications of global SuperDARN convection measurements, *Geophys. Res. Lett.*, *35*, L09102, doi:10.1029/2008GL033671.
Mende, S. B., et al. (2000a), Far ultraviolet imaging from the IMAGE spacecraft. 1. System design, *Space Sci. Rev.*, *91*, 243–270.
Mende, S. B., et al. (2000b), Far ultraviolet imaging from the IMAGE spacecraft. 2. Wideband FUV imaging, *Space Sci. Rev.*, *91*, 271–285.
Mende, S. B., et al. (2000c), Far ultraviolet imaging from the IMAGE spacecraft. 3. Spectral imaging of Lyman-α and OI 135.6 nm, in *The IMAGE Mission*, edited by J. L. Burch, chap. 3, pp. 287–318, Springer, Netherlands, doi:10.1007/978-94-011-4233-5_10.
Mende, S. B., H. U. Frey, B. J. Morsony, and T. J. Immel (2003), Statistical behavior of proton and electron auroras during substorms, *J. Geophys. Res.*, *108*(A9), 1339, doi:10.1029/2002JA009751.
Meng, C.-I., and K. Liou (2004), Substorm timings and timescales: A new aspect, *Space Sci. Rev.*, *113*(1–2), 41–75, doi:10.1023/B:SPAC.0000042939.88548.68.
Milan, S. E. (2015), *Sun et Lumière: Solar Wind-magnetosphere Coupling as Deduced from Ionospheric Flows and Polar Auroras*, pp. 33–64, Springer, Cambridge, U. K., doi:10.1007/978-3-319-18359-6_2.
Milan, S. E., M. Lester, S. W. H. Cowley, K. Oksavik, M. Brittnacher, R. A. Greenwald, G. Sofko, and J.-P. Villain (2003), Variations in the polar cap area during two substorm cycles, *Ann. Geophys.*, *21*, 1121–1140.
Milan, S. E., J. A. Wild, B. Hubert, C. M. Carr, E. A. Lucek, J. M. Bosqued, J. F. Watermann, and J. A. Slavin (2006), Flux closure during a substorm observed by Cluster, Double Star, IMAGE FUV, SuperDARN, and Greenland magnetometers, *Ann. Geophys.*, *24*(2), 751–767, doi:10.5194/angeo-24-751-2006.
Milan, S. E., G. Provan, and B. Hubert (2007), Magnetic flux transport in the Dungey cycle: A survey of dayside and nightside reconnection rates, *J. Geophys. Res.*, *112*, A01209, doi:10.1029/2006JA011642.
Milan, S. E., J. Hutchinson, P. D. Boakes, and B. Hubert (2009), Influences on the radius of the auroral oval, *Ann. Geophys.*, *27*, 2913–2924.
Milan, S. E., T. A. Evans, and B. Hubert (2010), Average auroral configuration parameterized by geomagnetic activity and solar wind conditions, *Ann. Geophys.*, *28*(4), 1003–1012, doi:10.5194/angeo-28-1003-2010.
Milan, S. E., J. S. Gosling, and B. Hubert (2012), Relationship between interplanetary parameters and the magnetopause reconnection rate quantified from observations of the expanding polar cap, *J. Geophys. Res.*, *117*, A03226, doi:10.1029/2011JA017082.
Murphy, K. R., I. R. Mann, I. J. Rae, C. L. Waters, H. U. Frey, A. Kale, H. J. Singer, B. J. Anderson, and H. Korth (2013), The detailed spatial structure of field-aligned currents comprising the substorm current wedge, *J. Geophys. Res. Space Physics*, *118*, 7714–7727, doi:10.1002/2013JA018979.
Newell, P. T., and J. W. Gjerloev (2011), Evaluation of SuperMAG auroral electrojet indices as indicators of substorms and auroral power, *J. Geophys. Res.*, *116*, A12211, doi:10.1029/2011JA016779.
Newell, P. T., K. Liou, T. Sotirelis, and C.-I. Meng (2001), Auroral precipitation power during substorms: A Polar UV imager-based superposed epoch analysis, *J. Geophys. Res.*, *106*(A12), 28,885–28,896, doi:10.1029/2000JA000428.
O'Brien, T. P., S. M. Thompson, and R. L. McPherron (2002), Steady magnetospheric convection: Statistical signatures in the solar wind and *AE*, *Geophys. Res. Lett.*, *29*(7), 1130, doi:10.1029/2001GL014641.
Partamies, N., T. I. Pulkkinen, R. L. McPherron, K. McWilliams, C. R. Bryant, E. Tanskanen, H. J. Singer, G. D. Reeves, and M. F. Thomsen (2009), Different magnetospheric modes: Solar wind driving and coupling efficiency, *Ann. Geophys.*, *27*(11), 4281–4291.
Perreault, P., and S.-I. Akasofu (1978), A study of geomagnetic storms, *Geophys. J. R. Astron. Soc.*, *54*, 547–573.
Pulkkinen, T. I., N. Partamies, R. L. McPherron, M. Henderson, G. D. Reeves, M. F. Thomsen, and H. J. Singer (2007), Comparative statistical analysis of storm time activations and sawtooth events, *J. Geophys. Res.*, *112*, A01205, doi:10.1029/2006JA012024.
Pulkkinen, T. I., M. Palmroth, H. E. J. Koskinen, T. V. Laitinen, C. C. Goodrich, V. G. Merkin, and J. G. Lyon (2010), Magnetospheric modes and solar wind energy coupling efficiency, *J. Geophys. Res.*, *115*, A03207, doi:10.1029/2009JA014737.

Pytte, T., R. L. McPherron, E. W. Hones, and H. I. West (1978), Multiple-satellite studies of magnetospheric substorms: Distinction between polar magnetic substorms and convection-driven negative bays, *J. Geophys. Res.*, *83*(A2), 663–679.

Richmond, A. D., and Y. Kamide (1988), Mapping electrodynamic features of the high-latitude ionosphere from localized observatories: Technique, *J. Geophys. Res.*, *93*(A6), 5741–5759.

Sergeev, V. A., E. M. Sazhina, N. A. Tsyganenko, J. A. Lundblad, and F. Soraas (1983), Pitch-angle scattering of energetic protons in the magnetotail current sheet as the dominant source of their isotropic precipitation into the nightside ionosphere, *Planet. Space Sci.*, *31*(10), 1147–1155, doi:10.1016/0032-0633(83)90103-4.

Sergeev, V. A., W. Lennartsson, R. Pellinen, M. Vallinkoski, and N. I. Fedorova (1990), Average patterns of precipitation and plasma flow in the plasma sheet flux tubes during steady magnetospheric convection, *Planet. Space Sci.*, *38*(3), 355–363, doi:10.1016/0032-0633(90)90101-U.

Sergeev, V. A., R. J. Pellinen, and T. I. Pulkkinen (1996), Steady magnetospheric convection: A review of recent results, *Space Sci. Rev.*, *75*, 551–604.

Sergeev, V. A., M. V. Kubyshkina, K. Liou, P. T. Newell, G. Parks, R. Nakamura, and T. Mukai (2001), Substorm and convection bay compared: Auroral and magnetotail dynamics during convection bay, *J. Geophys. Res.*, *106*(A9), 18,843–18,855, doi:10.1029/2000JA900087.

Shukhtina, M. A., and S. E. Milan (2014), ECLAT system level data product report (D430.1), *Tech. Rep. 2001*, Univ. of Leicester, U. K., doi:10.1007/978-90-481-3499-1.

Siscoe, G. L., and T. S. Huang (1985), Polar cap inflation and deflation, *J. Geophys. Res.*, *90*(A1), 543–547.

Walach, M.-T., and S. E. Milan (2015), Are steady magnetospheric convection events prolonged substorms?, *J. Geophys. Res. Space Physics*, *120*, 1751–1758, doi:10.1002/2014JA020631.

Yang, J., F. R. Toffoletto, and Y. Song (2010), Role of depleted flux tubes in steady magnetospheric convection: Results of RCM-E simulations, *J. Geophys. Res.*, *115*, A00111, doi:10.1029/2010JA015731.